Linear scaling computation of the Fock matrix. VII. Periodic density functional theory at the Γ point

C. J. Tymczak[a] and Matt Challacombe

Theoretical Division, Los Alamos National Laboratory, Los Alamos, New Mexico 87545

Linear scaling quantum chemical methods for density functional theory are extended to the condensed phase at the Γ point. For the two-electron Coulomb matrix, this is achieved with a tree-code algorithm for fast Coulomb summation [M. Challacombe and E. Schwegler, J. Chem. Phys. **106**, 5526 (1997)], together with multipole representation of the crystal field [M. Challacombe, C. White, and M. Head-Gordon, J. Chem. Phys. **107**, 10131 (1997)]. A periodic version of the hierarchical cubature algorithm [M. Challacombe, J. Chem. Phys. **113**, 10037 (2000)], which builds a telescoping adaptive grid for numerical integration of the exchange-correlation matrix, is shown to be efficient when the problem is posed as integration over the unit cell. Commonalities between the Coulomb and exchange-correlation algorithms are discussed, with an emphasis on achieving linear scaling through the use of modern data structures. With these developments, convergence of the Γ-point supercell approximation to the **k**-space integration limit is demonstrated for MgO and NaCl. Linear scaling construction of the Fockian and control of error is demonstrated for RBLYP/6-21G* diamond up to 512 atoms. © *2005 American Institute of Physics*. [DOI: 10.1063/1.1853374]

I. INTRODUCTION

Quantum chemical methods that employ Gaussian-type atomic orbitals (GTAOs) offer a number of advantages in materials science. First, because they are local basis functions, it is possible to achieve a linear scaling cost with system size for insulating systems. Second, almost all one- and two-electron integrals involving GTAOs are analytic, enabling the rapid evaluation of expectation values involving complicated operators that are often involved in the computation of response properties.[1–3] The Dalton quantum chemical program[4] is a premier example of this capability, offering a wide range of electric and magnetic molecular response properties. The ability to treat core-states analytically also opens the ability to go beyond the pseudopotential approximation in computation of relativistic effects with the four-component Dirac–Hartree–Fock[5,6] and Dirac–Kohn–Sham[7] theories. Perhaps most important though, the exact Hartree–Fock (HF) exchange may be computed efficiently with a GTAO basis set. In addition to providing a reference for correlated wave function methods, the exact HF exchange is central to hybrid HF/DFT models.[8–11] The use of hybrid methods in the condensed phase, pioneered by the CRYSTAL group,[12] has proven to be a useful improvement beyond the generalized gradient approximation for a number of properties, including bulk geometries, electronic properties,[13,14] and absorption energies.[15,16]

Recently, we have developed linear scaling quantum chemical methods for gas phase density functional theory (DFT), including computation of the Coulomb matrix **J** (Ref.

17) and the exchange-correlation matrix $\mathbf{K}_{xc}$.[18] In this contribution, these linear scaling methods are extended to periodic boundary conditions at the Γ point.

With periodic linear scaling quantum chemical algorithms, it is possible to begin bridging the gap between methods developed for small molecule chemistry and large scale problems in the solid state. Together with the results presented here, $O(N)$ methods for solving the Self-consistent-field equations[19,20] and linear scaling algorithms for computing the periodic HF exchange,[21] it is now possible to perform condensed phase HF/DFT calculations on systems larger than 500 atoms with a single processor. In addition, with the advent of linear scaling density matrix perturbation theory,[22,23] well developed quantum chemical methods for the analytic computation of response properties may be brought to bear on large solid state problems.

This paper is organized as follows: In Sec. II, periodic boundary conditions and the Γ-point approximation are introduced. Next, in Sec. III, the relationship between the numerical error estimates and data structures that underly the fast linear scaling algorithms for computation of the Coulomb and exchange-correlation matrix are outlined. In Sec. IV, we extend previous work on the Niboer and De Wette[24,25] lattice sum method to linear scaling computation of quantum Coulomb sums and tin-foil boundaries. Then, in Sec. V, $O(N)$ methods for computing the GTAO-based exchange-correlation matrix are presented. In Sec. VI A we discuss the implementation of these developments in the MONDOSCF[26] suite of linear scaling quantum chemistry codes. In Sec. VI B comparison of the Γ-point results is made with those obtained with CRYSTAL98 using **k**-space integration for NaCl and MgO. Next, in Sec. VI C, linear scaling is demonstrated for construction of the diamond Fock matrix at the

---
[a]Electronic mail: tymczak@lanl.gov

RBLYP/6-21G* level of theory. Finally, in Sec. VII we present our conclusions.

II. PERIODIC BOUNDARY CONDITIONS, LINEAR SCALING, AND BASIS SETS

In the conventional implementations of periodic boundary conditions, the Bloch functions

$$\psi_a^{\mathbf{k}}(\mathbf{r}) = \sum_{\mathbf{R}} e^{i\mathbf{k}\cdot\mathbf{R}} \phi_a(\mathbf{r}-\mathbf{R}) \tag{1}$$

are often constructed from nonorthogonal functions local to the unit cell (UC). Here, the local function ϕ_a is a GTAO centered on atom $\mathbf{A}$, while the sum on $\mathbf{R}$ runs over the Bravais lattice defined by integer translates of the primitive lattice vectors $\mathbf{a}$, $\mathbf{b}$, and $\mathbf{c}$. These Bloch functions (crystal orbitals) yield all possible translational symmetries through variation of the reciprocal lattice vector $\mathbf{k}$. Programs such as CRYSTAL98 perform a careful sampling of reciprocal space to achieve an accurate description of the periodic system. An alternative approach to including these important symmetries is to set $\mathbf{k}=0$, and then use a larger supercell created through replication and translation of the primitive unit cell. This is the supercell Γ-point approximation, used primarily for the study of defects and vacancies rather than as a replacement for $\mathbf{k}$-space integration.

In this contribution, $O(N)$ algorithms are developed specifically for the Γ-point approximation, allowing the use of large supercells in the case of high symmetry, as well as large primary cells in the case of disordered systems. While $\mathbf{k}$ dependence is avoided, lattice summation and formal integration over the unit cell volume V_{UC} are retained. At first sight this would seem to make matrix construction quite different than in the gas phase, where integrals are typically taken over all space, V_∞. Thus, elements of the gas phase overlap matrix,

$$S_{ab} = \int_{V_\infty} d\mathbf{r}\, \phi_a(\mathbf{r})\phi_b(\mathbf{r}), \tag{2}$$

become

$$S_{ab} = \sum_{\mathbf{R}-\mathbf{R}'} \int_{V_{\text{UC}}} d\mathbf{r}\, \phi_a(\mathbf{r}+\mathbf{R})\phi_b(\mathbf{r}+\mathbf{R}') \tag{3}$$

in the periodic Γ-point regime. However, this formalism can be brought into a form more closely related to its quantum chemical counterpart via the transformation,

$$\sum_{\mathbf{R}} \int_{V_{\text{UC}}} d\mathbf{r} f(\mathbf{r}+\mathbf{R}) \rightarrow \int_{V_\infty} d\mathbf{r} f(\mathbf{r}), \tag{4}$$

allowing use of conventional analytic integral technologies. For example, elements of the periodic overlap matrix become

$$S_{ab} = \sum_{\mathbf{R}} \int_{V_\infty} d\mathbf{r}\, \phi_a(\mathbf{r})\phi_b(\mathbf{r}+\mathbf{R}). \tag{5}$$

For compactness of notation, let us define the intermediate basis function products (distributions) $\rho_{ab}(\mathbf{r})=\Sigma_{\mathbf{R}\mathbf{R}'}\phi_a(\mathbf{r}+\mathbf{R})\phi_b(\mathbf{r}+\mathbf{R}')$ associated with integration over V_{UC} and the

corresponding distributions $\rho_{ab}^\infty(\mathbf{r})=\Sigma_{\mathbf{R}}\phi_a(\mathbf{r})\phi_b(\mathbf{r}+\mathbf{R})$ associated with integration over V_∞. We likewise define the electron density $\rho(\mathbf{r})=\Sigma_{ab}P_{ab}\rho_{ab}(\mathbf{r})$ associated with integration over V_{UC} and the corresponding density $\rho^\infty(\mathbf{r})=\Sigma_{ab}P_{ab}\rho_{ab}^\infty(\mathbf{r})$ associated with integration over V_∞, where P_{ab} is the one-electron reduced density matrix. In this convention, V_∞ is the default volume of integration, and elements of the periodic overlap matrix are expressed simply as $S_{ab}=\int d\mathbf{r}\rho_{ab}^\infty(\mathbf{r})$, while the electron count is $N_{\text{el}}=\int d\mathbf{r}\rho^\infty(\mathbf{r})$.

It is worth noting that the complexity of ρ^∞ is $O(N)$, due to the exponential prefactor $e^{-\chi_{ab}(\mathbf{A}-\mathbf{B}-\mathbf{R})^2}$ that enters each term in the sum over $\mathbf{A}$, $\mathbf{B}$, and $\mathbf{R}$. Thus, N scaling may be achieved *a priori* with a simple distance test. However, for small exponents, care must be exercised in truncation of periodic sums to avoid overlap matrices that are not positive definite. While these situations can often be ameliorated with a tighter distance neglect criteria, they are typically a symptom of near linear dependence, often due to the use of basis sets designed for gas phase calculations in conjunction with small unit cells.

These considerations and others are discussed by Towler in an excellent overview of Gaussian basis sets for the condensed phase.[27] Also, there are at least two (albeit related) libraries[28,29] of Gaussian basis sets appropriate for materials at standard densities. For high densities though, these basis sets may still encounter problems with linear dependence and sensitivity to truncation. One solution to this problem, suggested by Grüneich and Hess[30] for even tempered basis sets, is to scale the exponents by the inverse square of the lattice constant. In many cases though, especially for large systems, standard quantum chemical basis sets work well.

III. DATA STRUCTURES AND ERROR ESTIMATES

Both the quantum chemical tree code (QCTC) (Ref. 17) for computing the Coulomb matrix and Hierarchical Cubature (HiCu) (Ref. 18) for computing the exchange-correlation matrix are fast $O(N \ln N)$ algorithms whose performance is coupled to underlying data structures and error estimates. It is important to understand some of these particulars first, before addressing their extension to periodic boundary conditions. Also, the current version of QCTC is quite different from previous descriptions and deserves some introduction.

Both QCTC and HiCu are homeomorphic, involving k-d tree representation of the density. In our implementations, k-d trees are doubly linked lists with axis aligned bounding boxes (AABBs) delimiting the spatial *extent* of each node and its children. This scheme is similar to well developed technologies for ray tracing and data base searches, allowing fast $O(\ln N)$ *range queries* of overlapping components through AABB intersection tests.[31] In the case of QCTC, this fast look up constitutes the penetration acceptability criterion (PAC) which identifies spatial clusters or agglomerations ρ_Q of the density that may be accurately represented via a multipole approximation due to the absence of charge-charge penetration effects.

For accepted clusters a second test, the multipole acceptability criterion (MAC), is performed to check translation

errors in the multipole expansion. This second test is critical to the overall accuracy of the Coulomb matrix build. We have recently developed a different MAC in Ref. 32 that has several advantages. First, it takes into account the magnitude or weight of the distribution within the cluster. Second, it correctly takes into account the angular symmetry of the primitive Gaussian distributions. Third, and most important, it is always an exact bound to the translation error.

For each primitive bra distribution ρ_{ab}, a fast range query is performed on the k-d tree representation of the total density, leading to an on the fly partition of near-field (NF) and far-field (FF) interactions in construction of the gas phase Coulomb matrix which may be written as

$$J_{ab} = \sum_{Q \in \mathrm{FF}} \sum_l (-1)^l \sum_m O_m^l[\rho_{ab}] \sum_{l'} \sum_{m'} M_{m+m'}^{l+l'} O_{m'}^{l'}[\rho_Q]$$

$$+ \sum_{q \in \mathrm{NF}} \int d\mathbf{r} \int d\mathbf{r}' \rho_{ab}(\mathbf{r}) |\mathbf{r} - \mathbf{r}'|^{-1} \rho_q(\mathbf{r}), \quad (6)$$

where M_m^l is the irregular solid harmonic interaction tensor, $O_m^l[f] = \int d\mathbf{r} O_m^l(\mathbf{r}) f(\mathbf{r})$ is a moment of the regular solid harmonic, Q runs over the highest possible nodes in the density-tree consistent with the PAC and MAC, and q runs on left-over near-field primitive distributions in the density. See Refs. 17 and 33 for further details on this representation.

A fundamental difference between QCTC and FMM based methods is that QCTC pushes the near/far-field partition to the limit, employing the PAC and MAC best-case error estimates to resolve individual primitive distributions. On the other hand, FMM based methods employ static, worst-case error estimates. While recurring down the density tree to the level of individual primitives precludes well developed technologies for the integral evaluation of contracted functions, it accelerates the onset of linear scaling through early clustering.

The quantum chemical tree code generally employs the total density, which simplifies the code, allows electrostatic screening in MAC error estimates and provides charge neutrality, an essential feature for periodic calculations. Thus, the Coulomb matrix employed here includes the electron-nuclear terms; $\mathbf{J} \equiv \mathbf{J}_{ee} + \mathbf{V}_{en}$.

In the case of HiCu, two separate k-d tree structures are used. The rho-tree holds the electron density, while the cube-tree contains a hierarchical grid for integration of the exchange-correlation potential. Each node of the cube-tree is composed of a Cartesian nonproduct integration rule with the grid points enclosed by its AABB. The cube-tree is constructed iteratively through recursive bisection of the primary volume (the root AABB), using exact error bounds to achieve arbitrary precision of the integrated density and its gradients. As the cube-tree is extended, AABB intersection tests are performed while traversing the rho-tree, avoiding parts of the density that do not overlap with that portion of the grid. Upon construction of the grid, the reverse procedure is carried out; for each primitive distribution, the cube-tree is walked selecting only overlapping portions of the grid via the AABB intersection test.

For both of these fast algorithms, the trade-off between efficiency and accuracy is controlled by the AABB, which in turn depends on the the extent or range R_q of a primitive Gaussian distribution ρ_q, beyond which it is assumed to be negligible. Of course, negligible depends on the use to which the distribution is put, as will become obvious in the following.

Both HiCu and QCTC employ the Hermite–Gaussian representation of distributions[34]

$$\rho_q(\mathbf{r}) = \sum_{lmn} d_{lmn} \Lambda_{lmn}^q(\mathbf{r}), \quad (7)$$

where

$$\Lambda_{lmn}^q(\mathbf{r}) = \frac{\partial^{l+m+n}}{\partial Q_x^l \partial Q_y^m \partial Q_z^n} e^{-\zeta_q(\mathbf{r} - \mathbf{Q})^2}. \quad (8)$$

This representation provides an intermediate form into which elements of the density matrix may be folded, and allows the use of McMurchie–Davidson recurrence relations[35] in analytic integral evaluation and density evaluation. For this form, Cramer's inequality[36] provides a bound for the behavior of a Hermite–Gaussian distribution:

$$\rho_q(\mathbf{r}) \leq C_q e^{-\tilde{\zeta}_q(\mathbf{r} - \mathbf{Q})^2}, \quad (9)$$

where

$$C_q = \sum_{lmn} |d_{lmn}| K^3 [2^{l+m+n} l! m! n! \zeta_q^{l+m+n}]^{1/2}, \quad (10)$$

the constant $K = 1.09$, and

$$\tilde{\zeta}_q = \begin{cases} \zeta_q & l+m+n = 0 \\ \frac{1}{2}\zeta_q & \text{otherwise}. \end{cases} \quad (11)$$

The overlap extent R_q^o is the value beyond which numerical evaluation of the distribution ρ_q yields a value less than τ,

$$C_q e^{-\tilde{\zeta}_q(R_q^o)^2} = \tau. \quad (12)$$

For QCTC, errors in the electrostatic potential due to penetration errors must be considered. For this purpose, the penetration extent R_q^p is introduced, satisfying the equation

$$C_q \int [(\pi/\tilde{\zeta}_q)^{3/2} \delta(r) - e^{-\tilde{\zeta}_q r^2}] |r - R_q^p|^{-1} dr = \tau. \quad (13)$$

In both HiCu and QCTC, the density tree is constructed by recursively splitting the largest box dimension, until each primitive has been resolved. Then the primitive AABBs are computed from their extents and merged recursively back up the tree. For HiCu, this is all there is to it, but for QCTC multipole moments are also translated to a common center and recursively merged up the tree. Also, when computing matrix elements of $\mathbf{J}$, the primitive bra AABB is computed with R_q^o, while the R_q^p are used to construct AABBs of the density tree.

In Fig. 1, differences between the penetration and overlap extent are shown for a diffuse s-type Gaussian. For large extents, such as those encountered in a static FMM-type error bound, the two extents behave in a similar way. However, with aggressive use of the multipole approximation as in QCTC, the distinction becomes critical.
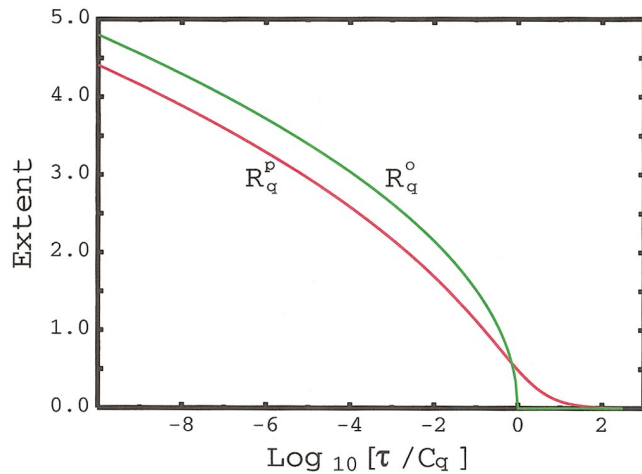
FIG. 1. (Color) Behavior of the overlap extent R^o and the penetration extent R^p as a function of τ/C_q for an s-type Gaussian with exponent $\zeta=1$. For small C_q (occurring, for example, due to a large atom-atom separation and/or small density matrix prefactor), R^o goes to zero at the origin and its distribution is eliminated, while R^p goes slowly to zero due to the Coulomb singularity.

IV. PERIODIC QUANTUM COULOMB SUMS

In the Γ-point approximation, elements of the periodic Coulomb matrix are

$$J_{ab} = \int_{V_{\mathrm{UC}}} d\mathbf{r} \int d\mathbf{r}' \rho_{ab}(\mathbf{r})|\mathbf{r}-\mathbf{r}'|^{-1}\rho_{\mathrm{tot}}(\mathbf{r}')$$

$$= \sum_{\mathbf{R}} \int \int d\mathbf{r}d\mathbf{r}' \rho_{ab}^{\infty}(\mathbf{r})|\mathbf{r}-\mathbf{r}'|^{-1}\rho_{\mathrm{tot}}^{\infty}(\mathbf{r}'+\mathbf{R}), \quad (14)$$

where ρ_{tot} is the total periodic density including both electronic and nuclear terms. These integrals involve infinite summation over the lattice vectors $\mathbf{R}$, and must be handled with care. There are at least two main approaches to handling this summation: Multipole expansion of the Ewald potential or Ewald-like summation of the multipole expansion. Expansion of the Ewald potential yields tin foil (TF) boundary conditions, requires reciprocal and real space summation with every $\mathbf{J}$ build, and scales as $O(N^{3/2})$. An alternative is the Ewald-like summation of the multipole interaction tensor, which was first described by Nijboer and De Wette (NDW) (Refs. 24 and 25) and later reviewed and extended by Challacombe, White, and Head–Gordon[33] to lattice summation of the irregular solid harmonic multipole interaction tensor. This Ewald-like summation is taken over the periodic far field V_{PFF} and is equivalent to a direct lattice summation (not a true Ewald sum) excluding an inner region V_{In} surrounding the unit cell. This inner region has been subtracted to avoid penetration errors and to guarantee convergence of the multipole expansion. With the summed interaction tensors cheaply precomputed and reused, the cost of Coulomb summation over the PFF scales as $O(Np^2)$, where p is the order of the multipole expansion. With this partition, the N-scaling periodic quantum Coulomb sums involve the contributions
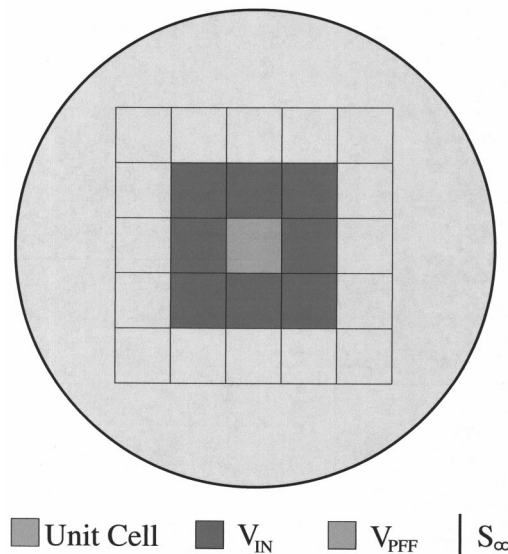

FIG. 2. Schematic of the regions contributing to N-scaling summation of the Coulomb matrix. The inner cells that make up V_{In} provide a buffer region that guarantees convergence of the multipole expansion of Coulomb interactions between the unit cell and all cells in V_{PFF}. The periodic far-field region V_{PFF} is the spherically ordered lattice extending to infinity but excluding V_{In}. For large cells and/or high order multipole expansions, V_{In} includes just the unit cell's 27 nearest neighbors. In FMM notation this corresponds to ws=1. However, for smaller cells and/or lower order multipole expansions, V_{In} tends to a spherical distribution of cells surrounding the unit cell. Direct summation over V_{PFF} leads to charges at the infinite surface S_{∞}, which must be be canceled by tin-foil (conducting) boundary conditions to achieve equivalence with Ewald summation.

$$\mathbf{J} = \mathbf{J}^{\mathrm{In}} + \mathbf{J}^{\mathrm{PFF}} + \mathbf{J}^{\mathrm{TF}}, \quad (15)$$

corresponding to the three separate regions shown in Fig. 2. Here, $\mathbf{J}^{\mathrm{In}}$ is computed using the fast $O(N \ln N)$ QCTC algorithm outlined previously in Sec. III. Construction of $\mathbf{J}^{\mathrm{PFF}}$ will be developed in the following section, while in Sec. IV B the term $\mathbf{J}^{\mathrm{TF}}$, necessary to introduce tin-foil boundary conditions, is detailed.

A. The periodic far field

By construction, the PFF term in the Coulomb matrix,

$$J_{ab}^{\mathrm{PFF}} = \sum_{\mathbf{R}\in\mathrm{PFF}} \int \int d\mathbf{r}d\mathbf{r}' \rho_{ab}^{\infty}(\mathbf{r})|\mathbf{r}-\mathbf{r}'+\mathbf{R}|^{-1}\rho_{\mathrm{tot}}^{\infty}(\mathbf{r}'),$$

$$(16)$$

involves charge distributions that are well separated with respect to both penetration and the convergence of multipole expansion errors, as outlined in Fig. 2 and discussed in the following.

With these conditions, and assuming the unit cell is centered at the origin, the bipolar multipole expansion employing the regular and irregular solid harmonics, O_m^l and M_m^l, respectively, is

$|\mathbf{r} - \mathbf{r'} + \mathbf{R}|^{-1}$

$$\approx \sum_{l=0}^{p} (-1)^l \sum_{l'=0}^{p} \left[\sum_{m=-l}^{l} \sum_{m=-l'}^{l'} O_l^m(\mathbf{r}) M_{l+l'}^{m+m'}(\mathbf{R}) O_{l'}^{m'}(\mathbf{r'}) \right].$$

(17)

Inserting Eq. (17) into Eq. (16) yields

$$J_{ab}^{PFF} = \sum_{\mathbf{R} \in PFF} \sum_{l=0}^{p} (-1)^l$$
$$\times \sum_{l'=0}^{p} \sum_{m=-l}^{l} \left(\sum_{m=-l'}^{l'} O_l^m[\rho_{ab}^\infty] M_{l+l'}^{m+m'}(\mathbf{R}) O_{l'}^{m'}[\rho_{tot}^\infty] \right).$$

(18)

This expression decouples the complexity of ρ_{ab}^∞ from ρ_{tot}^∞ through the precomputed multipole moments $O_l^m[\rho_{ab}^\infty] = \int d\mathbf{r} O_l^m(\mathbf{r}) \rho_{ab}^\infty(\mathbf{r})$ and $O_l^m[\rho_{tot}^\infty] = \int d\mathbf{r} O_l^m(\mathbf{r}) \rho_{tot}^\infty(\mathbf{r})$. Following Nijboer and De Wette,[24,25,33] we introduce the effective multipole interaction tensor

$$\mathcal{M}_l^m = \sum_{\mathbf{R} \in V_{PFF}} M_l^m(\mathbf{R}),$$

(19)

which can be efficiently computed on the fly for each new lattice, both to high accuracy and to high order (large p) using the new methods detailed in the Appendix. Note that this is a direct sum of the interaction tensor, and is *not* equivalent to Ewald summation. Nevertheless, with this simplification, the $O(p^2 N)$ working equation

$$J_{ab}^{PFF} = \sum_{l=0}^{p} \sum_{m=-l}^{l} O_l^m[\rho_{ab}^\infty] \mathcal{J}_l^m$$

(20)

is obtained, where the intermediate tensor

$$\mathcal{J}_m^l = (-1)^l \sum_{l'=0}^{p} \sum_{m=-l'}^{l'} \mathcal{M}_{l+l'}^{m+m'} O_{l'}^{m'}[\rho_{tot}^\infty]$$

(21)

is cheaply precomputed at the start of each Coulomb build.

Because Eq. (20) is inexpensive, our strategy is to define a minimal buffer region V_{In} sufficient to control penetration errors, subtracting effort from the computation of J^{In} via QCTC and replacing it with cheaper, multipole work in the computation of J^{PFF}. To this end, a fixed inner region V_{In} is constructed from neighboring cells that have simple Gaussian overlap with the unit cell, defined by the radius R^o. As explained in Sec. III, for the relatively large distances considered at this level the differences between the penetration and overlap extent are negligible. With V_{In} fixed, the precision of $\mathbf{J}^{PFF}$ is controlled entirely by the expansion order p. In general p will be much higher than the expansion order (~ 5) employed by QCTC in computation of $\mathbf{J}^{In}$. With QCTC accuracy is controlled on the fly by the MAC and PAC, establishing a dynamic near/far-field partition, while computation of $\mathbf{J}^{PFF}$ involves a static, worst-case error dominated by the multipole expansion. This static error is controlled by using the FMM-like error bound,

$$\frac{2^p \mathcal{C}^2 d_{max}^{p+1}}{(R^o)^{p+1} |R^o - 2 d_{max}|} \leq \tau_{MAC},$$

(22)

to set the appropriate expansion order p. In Eq. (22), d_{max} is the maximum translational distance, $\mathcal{C}$ is the asymptotic Unsöld weight of the total density, and τ_{MAC} is the threshold controlling the translation errors. See Ref. 32 for development of this expression and further explanation of these parameters.

B. Tin-foil boundary conditions

The surface charges created by direct summation over V_{PFF} must be canceled to achieve equivalence with Ewald summation. Achieving this equivalence is more than semantic, since without tin-foil boundary conditions matrix elements lack translational invariance and often incur dramatic charge sloshing instabilities. The correction is strongly dependent on ordering of the direct sum; as the Nijboer and De Wette method corresponds to spherical summation due to symmetry of the real/reciprocal space partition, the appropriate correction is[37]

$$\mathbf{\Phi}_{Ew}(\mathbf{r}) = \mathbf{\Phi}_{SS}(\mathbf{r}) + \frac{2\pi}{3 V_{UC}} (Q - 2\mathbf{r} \cdot \mathbf{D}),$$

(23)

where $\mathbf{D}$ is the system dipole moment, Q is trace of the system quadrupole, and we have assumed origin centering, the tin-foil correction to the Coulomb matrix is then

$$J_{ab}^{TF} = \frac{2\pi}{2 V_{UC}} (Q S_{ab} - 2\mathbf{d}_{ab} \cdot \mathbf{D}),$$

(24)

with S_{ab} being an element of the overlap matrix and $\mathbf{d}_{ab}$ the dipole moment of the distribution ρ_{ab}^∞.

V. PERIODIC EXCHANGE CORRELATION

The HiCu algorithm is ideally suited for periodic boundary conditions, as the unit-cell V_{UC} can be simply transformed into an equivalent rectangular integration domain $V_\square$, that is, the cube-tree's AABB. These volumes, shown in Fig. 3, are equivalent due to full periodicity of both distributions and density. The integration is then simply

$$K_{ab}^{xc} = \int_{V_\square} d\mathbf{r} \rho_{ab}(\mathbf{r}) v_{xc}[\rho; \mathbf{r}].$$

(25)

This approach should be contrasted with more conventional quantum chemical methods for computing the exchange-correlation matrix, involving the "Becke weights,"[38] which demand numerical integration over V_∞.

While we have written Eq. (25) in terms of the exchange-correlation potential for simplicity, in practice HiCu employs the Pople, Gill, and Johnson formulation.[18,39]

Because the distributions and density both involve a double sum over lattice vectors, there will be a large number of atom-atom pairs that do not overlap with $V_\square$. A similar situation is encountered in the gas phase for parallel versions of HiCu,[40] where each processor has a small, local cube-tree that may overlap only a few of the many possible atom-atom pairs. The solution to this problem again comes from the ray
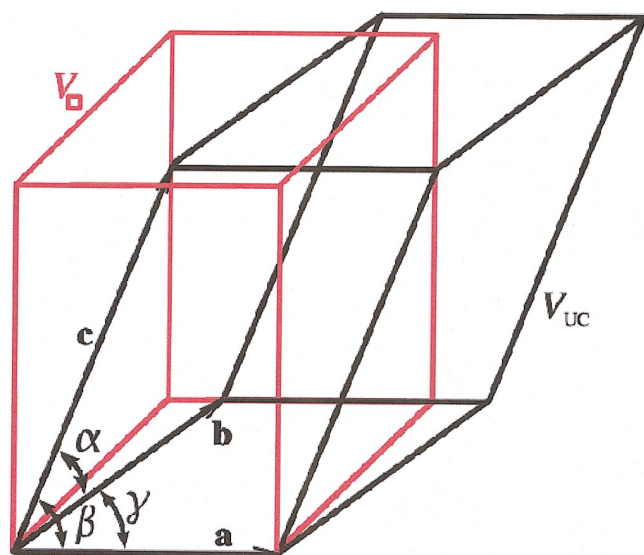
FIG. 3. (Color) Transformation between the unit cell with volume V_{UC} (described by the primitive lattice vectors **a**, **b**, and **c**) and the rectangular integration volume $V_{\square}$ employed by HiCu.

tracing literature, in the form of a modified ray-AABB (Ref. 31) and sphere-AABB test.[41] The ray-AABB test has been modified into a cylinder-AABB test, where the radius of the cylinder is a maximal overlap extent of the atom-atom pair. In the case of a same center atom-atom pair, it is of course more appropriate to employ a sphere-AABB test. In both cases, overlap between the HiCu integration volume and atom-atom pairs is established with a negligible prefactor when using these tests.

VI. RESULTS

A. Implementation

All developments were implemented in a serial version of MONDOSCF v1.0α9,[26] a suite of linear scaling quantum chemistry code. The code was complied using the Portland Group F90 compiler PGF90 V4.2 (Ref. 42) with the −01 −tp athlon options and with the Gnu C compiler GCC V3.2.2 using the −01 flag. All calculations were carried out on a 1.6 GHz AMD Athlon running REDHAT LINUXV9.0.[43]

Thresholds controlling the cost to accuracy ratio of HiCu and QCTC are set by the accuracy levels LOOSE, GOOD, and TIGHT, which have been empirically chosen to deliver 4–5, 6–7, and 8–9 digits, respectively, of relative accuracy in the energy. Values of these thresholds are listed in Appendix B of Ref. 21. The unmodified two-electron threshold τ_{2E} sets the overlap extent R_p^o in Eq. (12) and the penetration extent R_q^p in Eq. (13), both of which control the PAC. As explained in Ref. 32, the threshold τ_{MAC} controlling the MAC is set as $\tau_{MAC}=10^2\tau_{2E}$. The HiCu threshold τ_{HICU} likewise sets two subthresholds. The overlap extent R_p^o in Eq. (12), defining accuracy of the density on the grid, is set using $10^{-1}\tau_{HICU}$ (τ_ρ in Ref. 18). The target relative error defining accuracy of the HiCu grid is just τ_{HICU} (τ_r in Ref. 18). It should be pointed out that of all the thresholding schemes, those governing
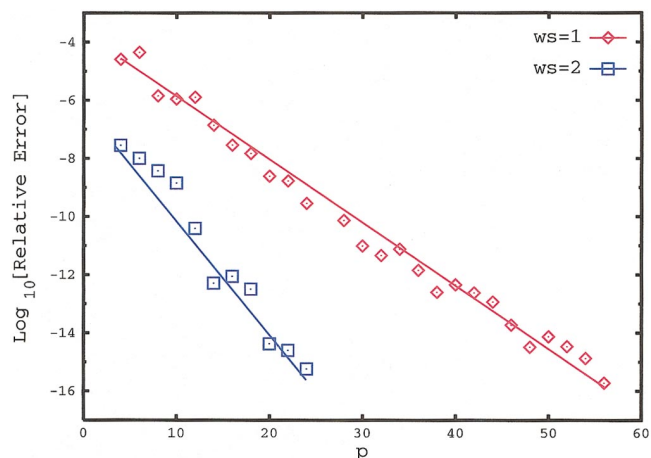

FIG. 4. (Color) Error in the Coulomb energy computed with the Nijboer and De Wette scheme relative to true Ewald summation. Shown is the error in the Coulomb energy vs p with one (ws=1) and two (ws=2) layers of cells in V_{PFF} for a periodic system of 64 classical water molecules.

HiCu are the least conservative; it is a simple (and not too expensive) matter to simply tighten the HiCu threshold if intermediate accuracies are required.

The multipole interaction and contraction code used by QCTC in the near/far-field partition has been highly optimized by symbolic manipulation and factorization, using real arithmetic and expansions through seventh order in the calculation of $\mathbf{J}^{In}$. The computation of $\mathbf{J}^{PFF}$ employs a general code for multipole contraction, allowing expansion through $p=64$. Eigensolution of the self-consistent-field equations has been used throughout, with the corresponding matrix and distribution thresholds given in Appendix B of Ref. 21. All calculations were performed with C_1 (no) symmetry, and all results are reported in atomic units.

B. Validation

The ability of our implementation to reproduce true Ewald summation is shown in Fig. 4 for a periodic system of 64 classical water molecules. Note that with both the Ewald sum and the Nijboer and De Wette approach, ordering the real and reciprocal space sums is critical; high order agreement is achieved only when the summation proceeds from the smallest to the largest terms.

The use of Cartesian Gaussian basis sets in many cases allows direct numerical comparison of different programs, at least to within the approximations, grids, etc., peculiar to a code. Here, we make connection with the preeminent Gaussian orbital program for periodic calculations, CRYSTAL98.[12]

TABLE I. Comparison of CRYSTAL98 and MONDOSCF Γ-point calculations on NaCl at the RBLYP/8-511/8-631G level of theory.

Program	N_{at}	Energy(a.u.)	Energy/N_{at}
MONODOSCF	2[a]	−622.391 01	−311.195 51
CRYSTAL98	2[a]	−622.391 14	−311.195 57
MONODOSCF	8[b]	−2490.0016	−311.250 20
CRYSTAL98	8[b]	−2490.0013	−311.250 16

[a]Triclinic.
[b]Cubic.

TABLE II. Convergence of the Γ-point supercell approximation for NaCl, computed with MONODOSCF at the RLDA/STO-3G level of theory.

Program	N_{at}	Energy (a.u.)	Energy/N_{at}
MONODOSCF	2[a]	−610.975 36	−305.487 68
	8[b]	−2444.3584	−305.544 80
	16[a]	−4888.7002	−305.543 77
	54[a]	−16 499.490	−305.546 11
	64[b]	−19 554.956	−305.546 18
	128[a]	−39 109.912	−305.546 18
	216[b]	−65 997.977	−305.546 19
CRYSTAL98[c]	2[a]	−611.092 28	−305.546 14

[a]Triclinic.
[b]Cubic.
[c]$6\times6\times6$ **k**-space grid.

TABLE IV. Convergence of the Γ-point supercell approximation for diamond, computed with MONODOSCF at the RBLYP/6-21G* level of theory.

N_{at}	Energy (a.u.)	Energy/N_{at}
8	−303.989	−37.9986
16	−608.667	−38.0417
32	−1218.02	−38.0632
64	−2436.28	−38.0669
96	−3654.59	−38.0687
144	−5482.04	−38.0697
216	−8223.10	−38.0699
288	−10964.1	−38.0700
384	−14618.9	−38.0700

7-f, we were not able to make a direct comparison for this basis set.

C. Scaling and accuracy

Demonstrating linear scaling at the outset, Fig. 5 shows the CPU time for **J** and $\mathbf{K}_{xc}$ builds with RBLYP/6-21G* diamond at its standard density. These timings correspond to a GOOD level of accuracy, targeting six digits in the total energy and corresponding to the values listed in Table IV. Shown in Fig. 6 is the precision of the computed energies, obtained by performing a second set of calculations with all thresholds reduced by one order of magnitude. For these calculations, the largest source of error is the numerical integration performed by HiCu, as the QCTC thresholds are significantly more conservative.

VII. CONCLUSIONS

We have extended linear scaling quantum chemical methods for computation of exchange-correlation and Coulomb matrices to periodic boundary conditions at the Γ point. These methods have demonstrated an early onset of linear scaling and error control for diamond, allowing calculations up to 512 atoms at the RBLYP/6-21G* level of theory. In both cases, this early onset of linear scaling has been enabled by the use of modern data structures such as the k-d tree, together with reliable error estimates for the Gaussian extent.
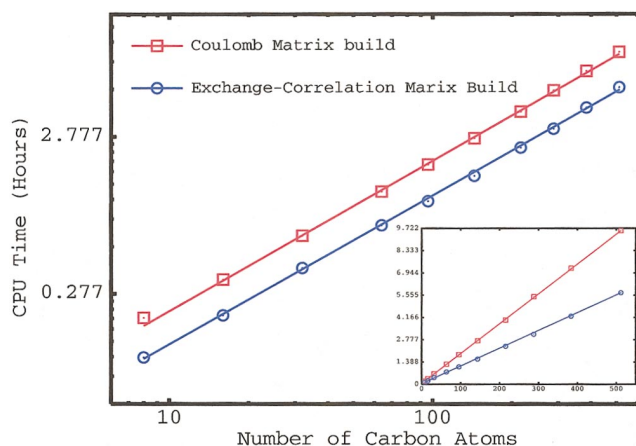
Calculations have been carried out largely with basis sets optimized for the condensed phase,[28] which tend to have less diffuse valence functions. Tables I–III make a direct comparison with CRYSTAL98 for NaCl and MgO obtained with the MONODOSCF TIGHT precision level. For the CRYSTAL98 calculations, we used the following threshold parameters: TOLDENS=10, TOLPOT=10, TOLGRID=15, and BASIS =4. The BASIS parameter determines the auxiliary functions used to fit the exchange-correlation potential.

In Table I, comparison is made for Γ-point NaCl with the 8-511G (Ref. 44) basis set for sodium, the 8-631G (Ref. 45) basis set for chlorine, and using the restricted BLYP functional.[46,47] Next, in Table II, convergence of the supercell Γ-point approximation is demonstrated for NaCl with the STO-3G basis set and the restricted local density approximation. Then, in Table III, convergence of the supercell Γ-point approximation to the **k**-space integration result is demonstrated for MgO, using the 8-61G (Ref. 48) basis set for magnesium, the 8-51G (Ref. 48) basis set for the oxygen, and the restricted BLYP functional. The primitive lattice coordinates for these systems are given in Ref. 49.

Finally, in Table IV, convergence of the supercell Γ-point approximation is shown for diamond at the GOOD accuracy level, using the restricted BLYP functional and the 6-21G* (Ref. 50) basis set. Since MONODOSCF employs 6-d and 10-f functions, while CRYSTAL98 employs 5-d and

TABLE III. Convergence of the Γ-point supercell approximation for MgO, computed with MONODOSCF at the RBLYP/8-61G/8-51G level of theory.

Program	N_{at}	Energy (a.u.)	Energy/N_{at}
MONODOSCF	2[a]	−275.090 97	−137.545 48
	8[b]	−1101.7295	−137.716 18
	16[a]	−2203.6904	−137.730 65
	54[a]	−7437.7989	−137.737 02
	64[b]	−8815.2131	−137.737 71
	128[a]	−17 630.430	−137.737 74
	216[b]	−29 751.352	−137.737 74
CRYSTAL98[c]	2[a]	−275.475 47	−137.737 74

[a]Triclinic.
[b]Cubic.
[c]$6\times6\times6$ **k**-space grid.

FIG. 5. (Color) Computational complexity of the **J** and $\mathbf{K}_{xc}$ matrix builds for cubic diamond at the RBLYP/6-21G* level of theory at the GOOD accuracy level.
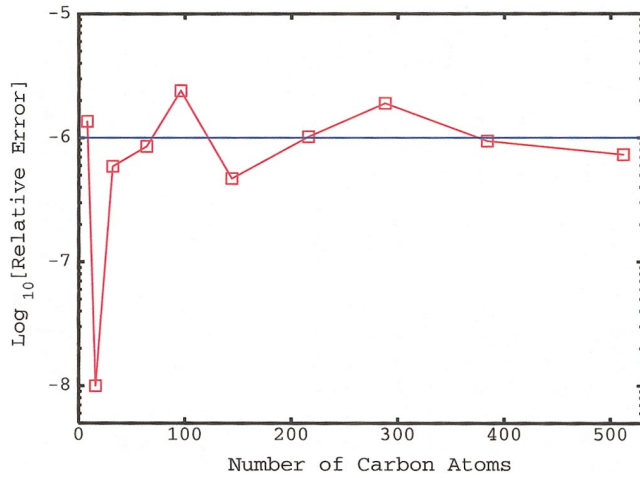
FIG. 6. (Color) Relative error with system size for RBLYP/6-21G* diamond at the GOOD accuracy level.

These algorithms have been parallelized,[40,51] demonstrating high efficiencies up to 128 processors, and have been used recently to determine the $T=0$ K equation of state for pentaerythritol tetranitrate[52] at the RPBE/6-31G** level of theory and a GOOD accuracy level.

While this contribution has focused on demonstrating linear scaling for diamond, the methods presented here work for slabs and wires as well, using methods for computation of the two- and one-dimensional the $\mathcal{M}$ tensor outlined in the Appendix. Our experience has shown that, for the same number of atoms, these lower dimensional systems run much faster.

APPENDIX: COMPUTATION OF THE $\mathcal{M}$ TENSOR

Following Nijboer and De Wette,[24,25] and later Challacombe, White, and Head–Gordon[33] (CWHG), we begin with the partition

$$\frac{1}{r^{l+1}} = \mathcal{G}_l(\beta,r) + \mathcal{F}_l(\beta,r) \tag{A1}$$

involving the functions

$$\mathcal{G}_l(\beta,r) = \frac{\Gamma\left(l+\frac{1}{2},\beta^2 r^2\right)}{\Gamma\left(l+\frac{1}{2}\right)r^{l+1}} \tag{A2}$$

and

$$\mathcal{F}_l(\beta,r) = \frac{\gamma\left(l+\frac{1}{2},\beta^2 r^2\right)}{\Gamma\left(l+\frac{1}{2}\right)r^{l+1}}, \tag{A3}$$

where Γ is the gamma function, γ is the incomplete gamma function,[53] and β is a parameter controlling the partition. With this separation of length scales, the lattice sum defining the multipole interaction tensor $\mathcal{M}_l^m$ may be expressed as

$$\mathcal{M}_l^m = \sum_{\mathbf{R} \in V_{PFF}} M_l^m[\mathbf{R}] = \sum_{\mathbf{R} \in V_{PFF}} \widetilde{P}_l^m(\cos\theta_{\mathbf{R}})e^{im\phi_{\mathbf{R}}}\mathcal{G}_l(\beta,|\mathbf{R}|)$$
$$+ \sum_{\mathbf{R} \in V_{PFF}} \widetilde{P}_l^m(\cos\theta_{\mathbf{R}})e^{im\phi_{\mathbf{R}}}\mathcal{F}_l(\beta,|\mathbf{R}|). \tag{A4}$$

Following CWHG, this expression can be further developed into real and reciprocal space terms:

$$\mathcal{M}_l^m = \sum_{\mathbf{R} \in V_{PFF}} \widetilde{P}_l^m(\cos\theta_{\mathbf{R}})e^{im\phi_{\mathbf{R}}}\mathcal{G}_l(\beta,|\mathbf{R}|)$$
$$- \sum_{\mathbf{R} \in V_{ln}} \widetilde{P}_l^m(\cos\theta_{\mathbf{R}})e^{im\phi_{\mathbf{R}}}\mathcal{F}_l(\beta,|\mathbf{R}|)$$
$$+ \frac{4\pi^{3/2}\left(\frac{i}{2}\right)^l}{V_{UC}\Gamma\left(l+\frac{1}{2}\right)} \sum_{\mathbf{G}\neq\{\varnothing\}} |\mathbf{G}|^{l-2}e^{-\pi^2|\mathbf{G}|^2/\beta^2}$$
$$\times \widetilde{P}_l^m(\cos\theta_{\mathbf{G}})e^{im\phi_{\mathbf{G}}}, \tag{A5}$$

where $\mathbf{G}$ are reciprocal lattice vectors. With an appropriate choice of $\beta \sim \sqrt{\pi}/(V_{UC})^{1/3}$, and summing terms from smallest to largest, the periodic multipole interaction tensor can be computed to high precision assuming an accurate representation of the incomplete gamma function. In previous work by CWHG, the upward recursion

$$\Gamma(m+1,x) = m\Gamma(m,x) + x^m e^{-x} \tag{A6}$$

was used, which results in a loss of precision for large values of x and m, demanding extended precision arithmetic and precluding on the fly computation. This problem is overcome by analytically summing the γ function, collecting terms, and then rewriting it as

$$\Gamma\left(m+\frac{1}{2},x\right) = \Gamma\left(m+\frac{1}{2}\right)\left\{\mathrm{erfc}(\sqrt{x})\right.$$
$$\left. + \sqrt{\frac{x}{\pi}}\sum_{n=0}^{m-1}(S_n x e^{-\pi/n})^n\right\}, \tag{A7}$$

where the terms

$$S_n = \left(\frac{\Gamma\left(\frac{1}{2}\right)}{\Gamma\left(n+\frac{3}{2}\right)}\right)^{1/\max(n,1)}, \tag{A8}$$

are simply pretabulated. This version of the γ function is both easy to program and precise, even for large values of x or m.

In one dimension, the $\mathcal{M}$ tensor can be computed analytically as

$$\mathcal{M}_l^m = \frac{\widetilde{P}_l^m(\cos\theta_0)e^{im\phi_0}}{a_0^{l+1}} \sum_{n=n_0}^{\infty} \frac{1}{n^{l+1}}$$

$$+ \frac{\widetilde{P}_l^m\left[\cos\left(\theta_0 + \frac{\pi}{2}\right)\right]e^{im(\phi_0+\pi)}}{a_0^{l+1}} \sum_{n=n_0}^{\infty} \frac{1}{n^{l+1}}$$

$$= Q_l^m[a_0,\theta_0,\phi_0]\left\{\zeta(l+1) - \sum_{n=1}^{n_0-1}\frac{1}{n^{l+1}}\right\}. \quad (A9)$$

where a_0, θ_0, and ϕ_0 are the initial box dimension and angles which are independent of the summation, and ζ is the Riemann zeta function.[53]

In two dimensions, the Fourier integrals for the calculation of the $\mathcal{M}$ tensor become more complicated. Taking the limit as the box dimension in the nonperiodic direction goes to infinity (the z direction in the following), we obtain from Eq. (A5)

$$\mathcal{M}_l^m = \sum_{\mathbf{R}\in V_{\text{PFF}}} (l-m)! P_l^m(\cos\theta_\mathbf{R})e^{im\phi_\mathbf{R}}\mathcal{G}_l(\beta,|\mathbf{R}|)$$

$$- \sum_{\mathbf{R}'\in V_{\text{ln}}} (l-m)! P_l^m(\cos\theta_\mathbf{R})e^{im\phi_\mathbf{R}}\mathcal{F}_l(\beta,|\mathbf{R}|)$$

$$+ \mathcal{C}_2 \sum_{\mathbf{G}\neq\{\varnothing\}} \int_{-\infty}^{\infty} dG_z |\mathbf{G}|^{l-2} e^{-\pi^2|\mathbf{G}|^2/\beta^2}\widetilde{P}_l^m(\cos\theta_\mathbf{G})e^{im\phi_\mathbf{G}},$$

$$(A10)$$

where

$$\mathcal{C}_2 = \frac{4\pi^{3/2}\left(\dfrac{i}{2}\right)^l}{A_{\text{UC}}\Gamma\left(l+\dfrac{1}{2}\right)} \quad (A11)$$

and A_{UC} is the area of the cell along the nonperiodic direction. In practice, we carry out numerical evaluation of this integral.

[1] M. Honda, K. Sato, and S. Obara, J. Chem. Phys. **94**, 3790 (1991).
[2] T. Helgaker and P. R. Taylor, Theor. Chim. Acta **83**, 177 (1992).
[3] P. J. Stephens, F. J. Devlin, C. F. Chabalowski, and M. J. Frisch, J. Phys. Chem. **98**, 11623 (1994).
[4] T. Helgaker, H. Jensen, P. Jorgensen *et al.*, DALTON, a molecular electronic structure program, Release 1.2, 2001, URL http://www.kjemi.uio.no/software/dalton/dalton.html
[5] J. K. Laerdahl, T. Saue, and K. Faegri, Theor. Chem. Acc. **97**, 177 (1997).
[6] I. P. Grant and H. M. Quiney, Int. J. Quantum Chem. **80**, 283 (2000).
[7] T. Yanai, H. Iikura, T. Nakajima, Y. Ishikawa, and K. Hirao, J. Chem. Phys. **115**, 8267 (2001).
[8] P. M. Gill, B. J. Johnson, J. A. Pople, and M. J. Frisch, Int. J. Quantum Chem. **S26**, 319 (1992).
[9] A. D. Becke, J. Chem. Phys. **98**, 1372 (1993).
[10] V. Barone, C. Adamo, and F. Mele, Chem. Phys. Lett. **249**, 290 (1996).
[11] C. Adamo, M. Cossi, and V. Barone, THEOCHEM **493**, 145 (1999).
[12] V. Saunders, R. Dovesi, C. Roetti, M. Causà, N. Harrison, R. Orlando, and C. M. Zicovich-Wilson, CRYSTAL98, http://www.chimifm.unito.it/teorica/crystal/ (1998).
[13] T. Bredow and A. R. Gerson, Phys. Rev. B **61**, 5194 (2000).
[14] J. Muscat, A. Wander, and N. M. Harrison, Chem. Phys. Lett. **342**, 397 (2001).
[15] P. Baranek, A. Lichanot, R. Orlando, and R. Dovesi, Chem. Phys. Lett. **340**, 362 (2001).
[16] A. Wander and N. M. Harrison, J. Chem. Phys. **105**, 6191 (2001).
[17] M. Challacombe and E. Schwegler, J. Chem. Phys. **106**, 5526 (1997).
[18] M. Challacombe, J. Chem. Phys. **113**, 10037 (2000).
[19] A. M. N. Niklasson, Phys. Rev. B **66**, 155115 (2002).
[20] A. M. N. Niklasson, C. J. Tymczak, and M. Challacombe, J. Chem. Phys. **118**, 8611 (2003).
[21] C. J. Tymczak, V. Weber, E. Schwegler, and M. Challacombe, Phys. Rev. B (submitted).
[22] A. M. N. Niklasson and M. Challacombe, Phys. Rev. Lett. **92**, 193001 (2004).
[23] V. Weber, A. M. N. Niklasson, and M. Challacombe, Phys. Rev. Lett. **92**, 193002 (2004).
[24] B. R. A. Nijboer and F. W. De Wette, Physica (Amsterdam) **23**, 309 (1957).
[25] B. R. A. Nijboer and F. W. De Wette, Physica (Amsterdam) **24**, 422 (1958).
[26] M. Challacombe, E. Schwegler, C. J. Tymczak, C. K. Gan, K. Nemeth, V. Weber, A. M. N. Niklasson, and G. Henkelman, MONDOSCF v1.0α9, A program suite for massively parallel, linear scaling SCF theory and ab initio molecular dynamics, 2001, URL http://www.t12.lanl.gov/home/mchalla/; Los Alamos National Laboratory Report No. LA-CC 01-2 (unpublished), Copyright University of California.
[27] M. Towler, *An introductory guide to Gaussian basis sets in solid-state electronic structure calculations* (2000), notes for Summer School, Torino.
[28] R. Dovesi, V. Saunders, C. Roetti, M. Causa, N. Harrison, R. Orlando, and C. Zicovich-Wilson, CRYSTAL98 *Basis Sets*, http://www.crystal.unito.it/Basis_Sets/ptable.html (2003).
[29] M. Towler, CRYSTAL98 *Basis Sets*, http://www.tcm.phy.cam.ac.uk/~mdt26/crystal.html (1998).
[30] A. Grüneich and B. A. Hess, Theor. Chem. Acc. **100**, 253 (1998).
[31] M. Gomez, Simple Intersection Tests for Games (1999), URL http://www.gamasutra.com/
[32] C. J. Tymczak and M. Challacombe (unpublished).
[33] M. Challacombe, C. White, and M. Head-Gordon, J. Chem. Phys. **107**, 10131 (1997).
[34] G. R. Ahmadi and J. Almlöf, Chem. Phys. Lett. **246**, 364 (1995).
[35] L. E. McMurchie and E. R. Davidson, J. Comp. Physiol. **26**, 218 (1978).
[36] E. Hille, Ann. Math. **27**, 427 (1926).
[37] A. Redlack and J. Grindlay, Can. J. Phys. **50**, 2815 (1972).
[38] A. D. Becke, J. Chem. Phys. **88**, 2547 (1988).
[39] J. A. Pople, P. M. W. Gill, and B. G. Johnson, Chem. Phys. Lett. **199**, 557 (1992).
[40] C. K. Gan and M. Challacombe, J. Chem. Phys. **118**, 9128 (2003).
[41] *Graphics Gems*, edited by A. S. Glassner (Academic, New York, 1990).
[42] The Portland Group, PGF90 V4.2 (2002), URL http://www.pgroup.com/
[43] Redhat, REDHAT V9.0, http://www.redhat.com/ (2004).
[44] M. Prencipe, A. Zupan, R. Dovesi, E. Apra, and V. R. Saunders, Phys. Rev. B **51**, 3391 (1995).
[45] N. M. Harrison and V. R. Saunders, J. Phys. I **4**, 3873 (1992).
[46] C. T. Lee, W. T. Yang, and R. G. Parr, Phys. Rev. B **37**, 785 (1988).
[47] A. D. Becke, Phys. Rev. A **38**, 3098 (1988).
[48] M. Causa, R. Dovesi, C. Pisani, and C. Roetti, Phys. Rev. B **33**, 1308 (1986).
[49] Periodic coordinates used in MONDOSCF validation (2004), URL http://www.t12.lanl.gov/~mchalla/
[50] M. Catti, A. Pavese, R. Dovesi, and V. R. Saunders, Phys. Rev. B **47**, 9189 (1993).
[51] C. K. Gan, C. J. Tymczak, and M. Challacombe, J. Chem. Phys. (to be published).
[52] C. K. Gan, T. D. Sewell, and M. Challacombe, Phys. Rev. B **69**, 035116 (2004).
[53] *Handbook of Mathematical Functions*, edited by M. Abramowitz and I. A. Stegun, 9th ed. (Dover, New York, 1987).